

PAPER

In situ exploration of the thermodynamic evolution properties in the type II interface from the WSe_2 - WS_2 lateral heterojunction

To cite this article: Ting Jiang *et al* 2018 *Nanotechnology* **29** 435703

View the [article online](#) for updates and enhancements.



IOP | ebooksTM

Bringing you innovative digital publishing with leading voices to create your essential collection of books in STEM research.

Start exploring the collection - download the first chapter of every title for free.

In situ exploration of the thermodynamic evolution properties in the type II interface from the WSe_2 – WS_2 lateral heterojunction

Ting Jiang¹, Fang Wang¹, Anyang Cui¹, Shuang Guo¹, Kai Jiang¹,
Liyang Shang¹, Zhigao Hu^{1,2}  and Junhao Chu¹

¹ Key Laboratory of Polar Materials and Devices (MOE) and Technical Center for Multifunctional Magneto-Optical Spectroscopy (Shanghai), Department of Electronic Engineering, East China Normal University, Shanghai 200241, People's Republic of China

² Collaborative Innovation Center of Extreme Optics, Shanxi University, Taiyuan, Shanxi 030006, People's Republic of China

E-mail: lyshang@ee.ecnu.edu.cn and zghu@ee.ecnu.edu.cn

Received 27 May 2018, revised 20 July 2018

Accepted for publication 10 August 2018

Published 23 August 2018



CrossMark

Abstract

The mutual interaction of the type II heterointerface can be very susceptible to the variation of electron states, introducing differences into the band structure and the band alignment in comparison to their pristine states. Here, the thermal evolution of the exciton transition and electronic properties inside the covalently bonded type II interface of the atomically planar WSe_2 – WS_2 lateral heterojunction has been studied. With the aid of luminescence and electronic evolution, it was found that the coupling at the heterointerface is strong, and that the change in the photon–electron transition with temperature is weak. Meanwhile, by employing some quantitative computational methods, the temperature variation of the extracted built-in electric field at the interface is unexpectedly pronounced, resulting from the thermodynamical spanning behaviors of the electrons, as well as the strains generated by the difference in the thermal expansion coefficient between the structural lattice. In addition, the electric contact at the interface shows a negative temperature correlation. The present findings provide a vital contribution to the photo–electron interaction-based application and evaluation paths of the electric contact in two-dimensional transition metal dichalcogenide-based devices.

Supplementary material for this article is available [online](#)

Keywords: WSe_2 – WS_2 lateral heterojunction, KPFM, Raman scattering, PL

(Some figures may appear in colour only in the online journal)

1. Introduction

Possessing several tunable properties, such as carrier density, band gap, band offset, and polarity, two-dimensional (2D) transition metal dichalcogenides (TMDCs) are regarded as promising candidates for applications in photoelectric and energy conversion devices [1–5]. Performance optimization, such as a faster response frequency or lower power dissipation, strongly relies on interfacial states, which are dominated by electronic behaviors, such as photon–electron coupling effects and the electron transfer process across the interface

[4, 5]. Previous works have realized the phase transition from semiconductor to metal of $MoTe_2$ thin films, and successfully reduced the Schottky contact barrier at the gold/TMDC interface [6–8]. In addition, a few groups have achieved low contact resistance between metallic graphene and other 2D materials [9]. Nevertheless, their practical applications were hindered by large scale fabrication [9, 10]. Luckily, large area lateral heterojunctions comprised of monolayer 2D TMDCs have been successfully grown recently [1, 2, 11–14]. As the milestone materials are of unique structures with two kinds of 2D TMDC materials covalently bonded at the interface, the

in-plane 2D lateral heterojunctions have evoked significant interest in the investigations of photoelectric properties and electric contacts at the interface [1, 12–17]. The interface of the 2D lateral heterojunctions exhibited typical p – n diode behaviors with remarkable electric properties of current rectification and photocurrent generation effects by the current–voltage (I/V) characterizations reported in previous works [1, 12–14, 16, 18–20]. However, the thermal-induced changes of the photon–electron interaction or band alignment properties, as well as the electronic distribution evolution at the heterointerface, have been seldom demonstrated in the 2D planar WSe_2 – WS_2 lateral heterojunction.

In this work, the coupling interaction of the covalently bonded interface and its *in situ* electronic properties in a monolayer WSe_2 – WS_2 lateral heterojunction have been systematically studied. By variable temperature tuning the electron transition, the band parameters change when the band structure is modulated. The location of the photon–electron interaction can effect the exciton transition energy of the interband, resulting in a blueshift of photo–excitons from a direct to indirect transition. The coupling strength for the covalently bonded interface is strong, which is revealed by the weak changes of photon energy. In addition, an *in situ* exploration is performed to gain direct insight into the thermodynamic electron evolution at the interface. It is found that temperature is a sensitive factor which specifically adjusts to the carrier distribution as well as the strains generated by the difference in the thermal expansion coefficient between the lattice. Furthermore, with quantitative computational methods, some associated parameters have also been extracted to evaluate the electric contact evolution. These investigations contribute to the estimation of the energy dissipation-induced thermogenesis in photoelectric devices, which can secure the long-term stability of the 2D TMDC-based circuit.

2. Experimental section

2.1. The growth of the WSe_2 – WS_2 lateral heterojunction

The 2D monolayer WSe_2 – WS_2 heterojunction was grown by a two-step epitaxial chemical vapor deposition method on an Si/SiO_2 substrate. Two quartz boats with WSe_2 and WS_2 powder were loaded into a horizontal tube furnace with a quartz tube. A clean Si/SiO_2 substrate was placed at the downstream end of the furnace as the growth substrate. The system was pump-purged with argon (Ar) gas and then ramped to the desired growth temperature for the growth of the WS_2 nanosheets at 1150 °C for 20 min under ambient pressure and a constant flow of 300 sccm Ar worked as the carrier gas. Then the boat with WS_2 powder was pushed out of the hot zone without breaking the vacuum, while the boat with WSe_2 powder was simultaneously pushed into the hot zone of the tube *in situ*. The temperature was then ramped to 1190 °C for the lateral epitaxial growth of the WSe_2 for about 20 min under 500 sccm Ar flow. Then the growth was terminated by shutting off the power of the furnace, and the sample was naturally cooled down to ambient temperature.

2.2. Microstructure exploration

The Raman scattering and photoluminescence (PL) measurements were implemented on a confocal microscope system (Jobin-Yvon LabRAM HR Evolution spectrometer) with a 532 nm excited laser. A grating of 1800 grooves mm^{-1} for Raman and 600 grooves mm^{-1} grating for PL was used to collect the spectral data. A THMSE 600 heating/cooling stage (Linkam Scientific Instruments) was used in the temperature range from 305 K–405 K with a resolution of 0.1 K. The topography and surface potential images of the sample were simultaneously obtained from the KPFM technique (Bruker, Dimension Icon SPM) in LiftMode, with dual-pass scanning. To avoid oxidation of the sample during the heating process, we performed all of the above in a dry N_2 atmosphere. Further, to arrive at the thermal equilibrium state of the charge transferring across the interface of the heterojunction, the temperature ascending speed was controlled at a rate of 5 K min^{-1} and temperature plateaus of 60 min. The tip bias was adjusted to cancel out the capacitive force by the KPFM system, according to the relation $\phi_{\text{sample}} = \phi_{\text{tip}} - e\text{CPD}$, where CPD represents the contact potential difference between the tip and sample and e is the elementary charge, respectively. The parameters ϕ_{sample} and ϕ_{tip} are the workfunctions of the sample and tip, respectively. The workfunction of the Pt/Ir-coated tip (ϕ_{tip}) was calibrated to be 4.48 eV using a freshly exfoliated surface of highly oriented pyrolytic graphite (HOPG), of which the workfunction (ϕ_{HOPG}) is assumed to be 4.47 eV [21]. The dimension heater/cooler could heat the sample from 300 K to 405 K with an accuracy of 1 K.

3. Results and discussion

3.1. Microstructure verification

Figure 1 shows the spatial distribution structures and optical properties of the planar WSe_2 – WS_2 lateral heterojunction. The optical contrast between the inner and outer triangle shows the core–shell structure of the WSe_2 – WS_2 lateral heterojunction. The AFM image ($85 \times 85 \mu\text{m}^2$) in figure 1(b) confirms that the WSe_2 – WS_2 heterojunction is monolayer, with a thickness of approximately 0.8 nm for the shell region and 0.6 nm for the core region, respectively. Figures 1(c)–(e) show the Raman images that map at 257.2 cm^{-1} corresponding to the A_{1g} resonant mode of WSe_2 and 338.1 cm^{-1} corresponding to the E_{2g}^1 resonant mode of WS_2 , respectively. PL intensity maps at 1.69 eV and 1.87 eV are further applied to characterize the distinct core–shell structure. We can clearly see that the PL peak around 1.87 eV is mainly localized at the inner layer (WS_2) while 1.69 eV for the outer layer (WSe_2). From figures 1(c)–(h), the spatial composition distribution within the WSe_2 – WS_2 heterojunction further verifies that the monolayer WSe_2 periphery region is laterally epitaxially connected with the edge of the monolayer WS_2 core region.

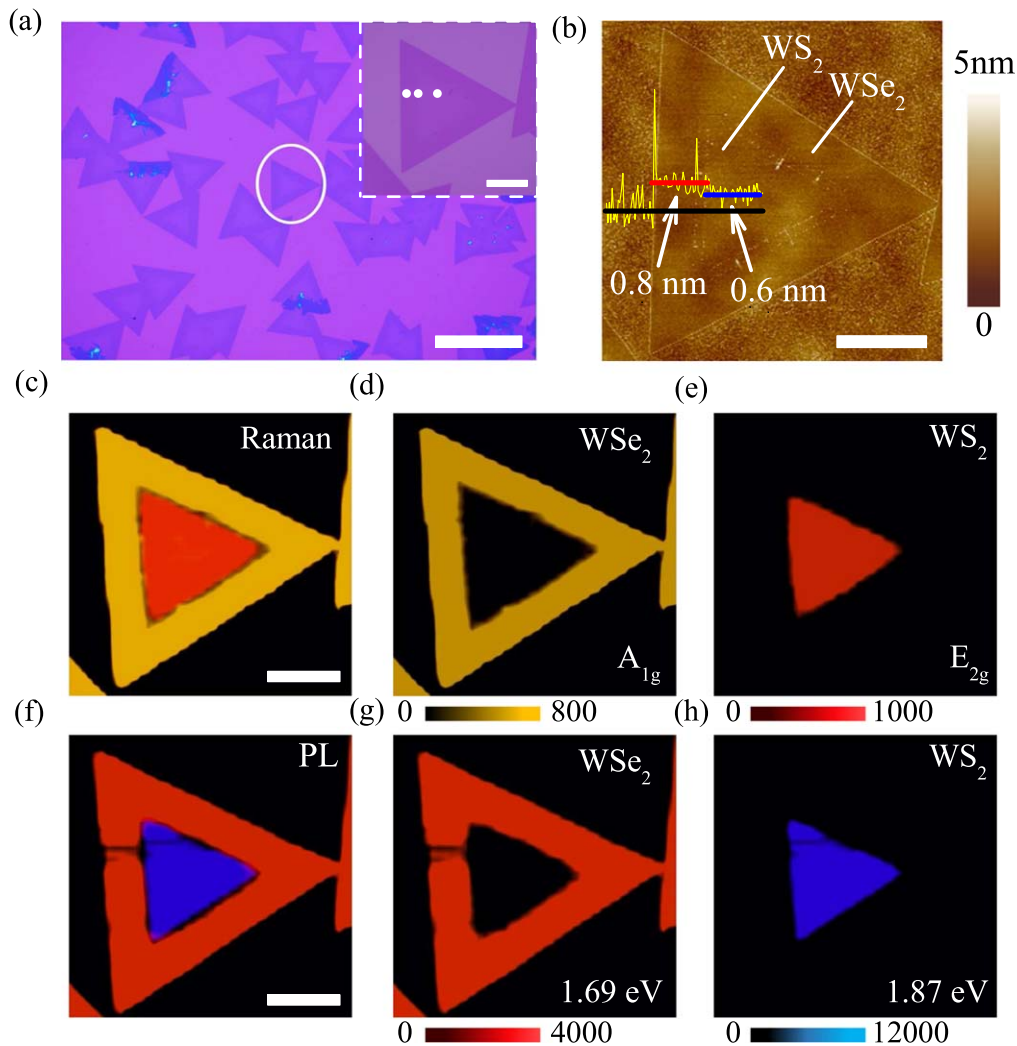


Figure 1. (a) Optical images of the WSe_2 - WS_2 heterostructure. The scale bar is $100\ \mu\text{m}$. The inset shows the circled zone. (b) AFM image of the monolayer WSe_2 - WS_2 heterostructure. Raman intensity maps at (d) $257.2\ \text{cm}^{-1}$ (A_{1g} resonant mode of WSe_2) and (e) $338.1\ \text{cm}^{-1}$ (E_{2g}^1 mode of WS_2). PL intensity maps at (g) $1.69\ \text{eV}$ of the outer WSe_2 and (h) $1.87\ \text{eV}$ of the inner WS_2 . (e), (f) The combined maps. Note that all the scale bars are limited to $20\ \mu\text{m}$.

3.2. Band structure evolution

Figure 2(a) shows the PL spectra taken from the point labeled in the inset of figure 1(a). The band structures at different positions in the heterojunction are distinct in the Gaussian fitting. The photon-excited electron-hole pairs will separate and relax to the conduction band edge of WSe_2 and the valence band edge of WS_2 , as shown in the schematic diagram of figure 3(a). The distinct peaks at 1.68 and $1.87\ \text{eV}$ correspond to the interband excitation for the pristine WSe_2 and WS_2 with a direct band gap, respectively. There is a gradual blueshift of the PL exciton position of pristine WSe_2 closing to the interface. Considering that the PL intensity of WS_2 is stronger than that of WSe_2 , this behavior in WS_2 is negligible. The profile shows that the exciton energy at the interface is approximately $60\ \text{meV}$ higher than that of the pristine WSe_2 district. However, the emission energy of pristine WS_2 is approximately $8\ \text{meV}$ higher than that of the interface region. Previous works have demonstrated that photon-electron interactions in semiconductor materials can

be seriously affected by chalcogen composition [22–24]. The optical properties of 2D TMDC alloy nanosheets, such as the band gap or the Raman frequency modes, can be varied linearly with stoichiometric compounds of a tunable sulfur ratio [23, 24]. Here, the prominent deviation of the PL emission energy between the pure and interface region in the WSe_2 - WS_2 heterojunction is presumably due to the mixed alloying of the chemical composition around the interface region. In other words, the S atoms are believed to coexist with Se atoms with a gradually changing stoichiometric ratio from pure WSe_2 or WS_2 to the alloying interface. Moreover, figure S1 (available online at stacks.iop.org/NANO/29/435703/mmedia) depicts the Raman spectra of the sample, which shows the peak positions shifting from pure WSe_2 or WS_2 to the interface region when the value of the $\Delta\omega_{A_{1g}}$ mode is $3.07\ \text{cm}^{-1}$ for WSe_2 and the $\Delta\omega_{E_{2g}}$ mode is $3.44\ \text{cm}^{-1}$, and the $\Delta\omega_{A_{1g}}$ mode is $1.99\ \text{cm}^{-1}$ for WS_2 , respectively. Therefore, the shifting behavior in both the PL and Raman spectra can confirm the hypothesis of the existence of a chemical composition transition region around the interface.

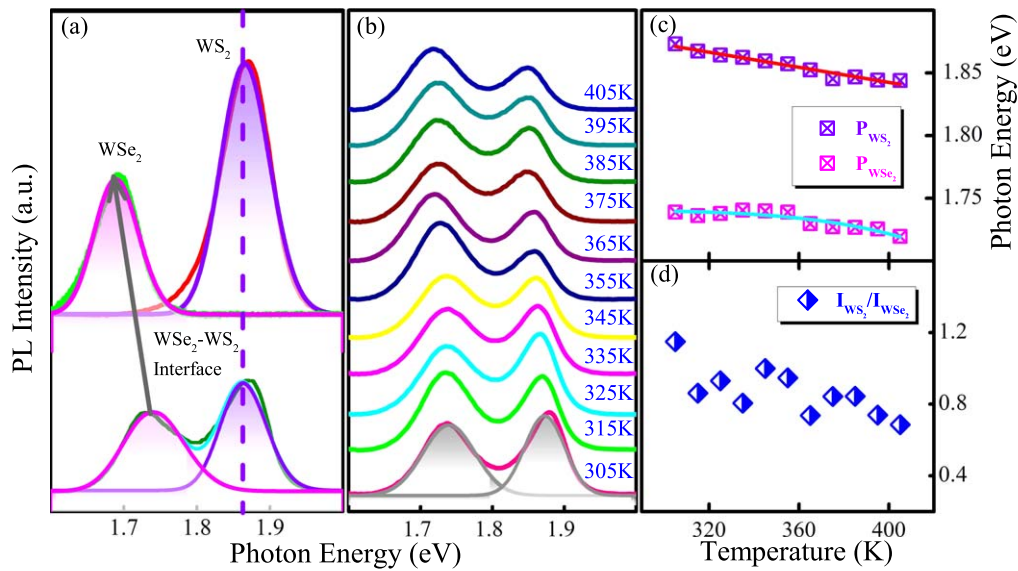


Figure 2. (a) The Gaussian fitting PL spectra of the WSe₂, WS₂ and the interface areas in the heterostructure domain as marked by the white dots in the inset of figure 1(a). (b) Normalized temperature-dependent PL spectra of the interface at the lateral heterostructure. (c) Peak position of WSe₂ and WS₂ extracted from the heterointerface. (d) The intensity ratios between WS₂ (I_1) and WSe₂ (I_2).

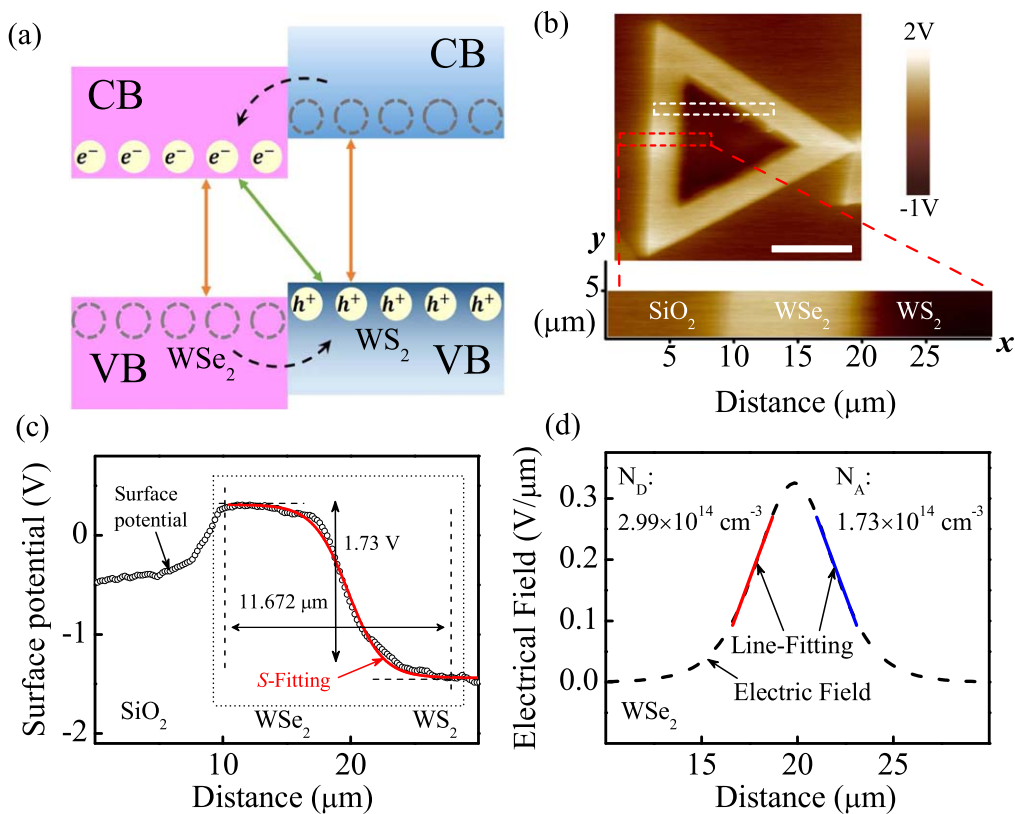


Figure 3. (a) Schematic diagrams of the band alignment of the WS₂-WSe₂ heterojunction. (b) The top panel is the surface potential image of the WS₂-WSe₂ heterostructure domain. The bottom panel is the selected area marked by a red dashed rectangular in the top panel for detailed analysis. Note that the scale bar is 20 μm . (c) Surface potential distribution at the WSe₂-WS₂ interface and its sigmoid function fitting curve. (d) Built-in electric field distribution at the interface of the WS₂-WSe₂ heterojunction.

The detailed temperature evolution of the electron transition for the covalently bonded interface in the WSe₂-WS₂ heterojunction is shown in figure 2(b). The photon energy of WSe₂ (P_{WSe_2}), WS₂ (P_{WS_2}) is fitted with the integrated intensity peak, on purpose to describe the intensity

variation trend with temperature. Figure 2(b) displays the luminescence intensity evolution of the heterointerface as a function of temperature from 305 K–405 K with a stability of about 0.1 K. The PL spectra can be deconvoluted into two major peaks. Along with the variation of the luminescent

Table 1. The parameter values of the modified Varshni model for peak energy at the interface as a function of temperature in figure 2(c).

Sample	Exciton	E_0 (eV)	S	$\langle \hbar \Delta \rangle$ (meV)
WSe ₂ -WS ₂	P _{WS₂}	1.96	3.43	8.13
Interface	P _{WSe₂}	1.74	2.78	6.23

intensity, the direct transition in the heterostructures experiences a gradual redshift as the temperature increases, as shown in figure 2(c). Such behavior is similar to the response of conventional semiconductors under high temperature, which can be attributed to increased phonon-exciton interactions and slight changes in bonding lengths. Thus, it provides a route to evaluate temperature correlations to the semiconductors. The temperature dependence of the PL peak position is fitted by employing the modified Varshni relationship:

$$E(T) = E_0 - S \langle \hbar \Delta \rangle \left[\cot h \frac{\langle \hbar \Delta \rangle}{2k_B T} - 1 \right] \quad (1)$$

where E_0 is the emission energy at zero absolute temperature, S is the Huang-Rhys factor which can reflect the coupling strength between the exciton and phonon, $\langle \hbar \Delta \rangle$ is the average phonon energy, and \hbar and k_B are the Plancks and Boltzmann constant, respectively. The fitting values of E_0 , S , and $\langle \hbar \Delta \rangle$ of WSe₂, WS₂ are extracted in table 1. By comparing the fitting parameters of the TMDCs at the interface, such as S , the contribution of the interface coupling can be informed. In addition, the temperature difference between WSe₂, WS₂ at the interface can also be derived by comparing the measured difference between the emission PL energy. The variation with temperature of the peak P_{WSe₂} and P_{WS₂} at the interface do not display a redshift as obvious as in the pristine WSe₂, WS₂ monolayer, which is a reflection of the strong coupling interaction between the exciton and phonon at the covalently bonded interface. Furthermore, the intensity ratio (I_{WS_2}/I_{WSe_2}) has been plotted to reflect the competing evolution of the exciton quantities between WSe₂ and WS₂ in variable temperature processes. The decrease of the intensity ratios, as shown in figure 2(d), also represents the direct-indirect spectral-weight conversion with the increasing temperature.

3.3. The electron states evolution

Figure 3(a) schematically depicts the type II band structures of the covalently bonded interface. From the surface potential image in figure 3(b), the workfunction of the shell WSe₂ is lower than that of the core WS₂. The discriminating difference between the Fermi levels of these two materials, which forms the built-in potential barrier, can facilitate the photo-excited electron-hole separation and verify the type II band alignment with an atomically sharp heterointerface. Neglecting the hybridization of electronic states in the WSe₂ and WS₂ layers, the lowest conduction band resides in WSe₂ and the highest valence band resides in WS₂, respectively [12, 16, 18, 20, 25]. Likewise, in the WSe₂-WS₂

heterostructure, due to type-II band alignment, photo-excited electrons and holes will relax (dashed lines in figure 3(a)) to the conduction band edge of WSe₂ and the valence band edge of WS₂, respectively.

As shown in figure 3(c), the value of the surface potential is averaged along the y -axis direction in the bottom panel of figure 3(b) under the thermal equilibrium condition, from which we can conclude that the WSe₂-WS₂ heterojunction serves as a quasi planar n - p junction, where the WSe₂ works for the n -side and WS₂ for the p -side. Treating the surface potential distribution with a sigmoid fitting function (S -fitting) below: [26, 27]

$$y = \frac{A_1 - A_2}{1 + e^{(x-x_0)/dx}} + A_2. \quad (2)$$

Here, $A_1 = 0.281$ and $A_2 = -1.433$; $dx = 1.083$ and $x_0 = 9.242 \mu\text{m}$ form the frontier between the quasi p -type region and n -type region, respectively. The distinction between the inherent Fermi levels of WSe₂ and WS₂ (ΔE_F) can be calculated by estimating the CPD difference between the WSe₂ and WS₂ sides ($\Delta\text{CPD}_{WSe_2-WS_2}$):

$$\Delta E_F = E_{F_{WSe_2}} - E_{F_{WS_2}} = \phi_{WS_2} - \phi_{WSe_2} = e\Delta\text{CPD}_{WSe_2-WS_2}. \quad (3)$$

Together with the S -fitting results, we can evaluate the value ΔE_F and the depletion region width to be approximately 1.73 eV and 11.67 μm , respectively. Meanwhile, the potential drop at the WSe₂/SiO₂ interface can be attributed to the abrupt height change, or the work function differences between semiconductor WSe₂ and insulator SiO₂ [28].

Furthermore, by differentiating the sigmoid fitting profile, we obtain the built-in electric field distribution, as shown in figure 3(d). The formed built-in electric field locates at the interface zone that impedes the dynamic diffusion of carriers. We use the below equations to define the built-in electric field distribution ($\xi(x)$) of the 2D abrupt junction: [29, 30]

$$\xi_{WSe_2}(x) \sim \frac{en_D(x - W_n)}{\epsilon_{WSe_2} \epsilon_0 \rho_{WSe_2}}, \quad (0 < x < W_n) \quad (4)$$

$$\xi_{WS_2}(x) \sim -\frac{en_A(x + W_p)}{\epsilon_{WS_2} \epsilon_0 \rho_{WS_2}}, \quad (-W_p < x < 0). \quad (5)$$

It is noteworthy that $\epsilon_{WS_2} = 6.1$ and $\epsilon_{WSe_2} = 11.7$ are the dielectric constant of monolayer WS₂ and WSe₂ [16, 19], respectively. The parameter ϵ_0 is the vacuum permittivity. ρ_{WSe_2} and ρ_{WS_2} are the screening lengths, given by $\rho_{WSe_2} = 2\pi\chi_{WSe_2}$ and $\rho_{WS_2} = 2\pi\chi_{WS_2}$, where $\chi_{WSe_2} = 0.718 \text{ nm}$ and $\chi_{WS_2} = 0.603 \text{ nm}$ are polarizabilities of monolayer WSe₂ and WS₂, respectively [31]. The maximum electric field is estimated to be 32.52 V cm⁻¹, almost locating at the midpoint of the depletion region. Moreover, the amount of the intrinsic doping concentration is derived from the slope of the linear fitting of the electric field distribution. It can be concluded that $n_D \approx 2.4 \times 10^7 \text{ cm}^{-2}$ in n -type WSe₂ and $n_A \approx 1.04 \times 10^7 \text{ cm}^{-2}$ in p -type WS₂, respectively. This result is reasonable when compared with the intrinsic carrier concentrations ($\sim 10^{10} \text{ cm}^{-2}$) reported in previous work [1, 16, 19]. Among which, W_n and W_p are the depletion width

in WSe₂ and WS₂, respectively. The total depletion width $W = W_n + W_p$, which is the varying part of the surface potential profile along the x -axis direction, can be obtained by the p - n junction modeling below: [19, 32]

$$W_p = \sqrt{\frac{2N_D \epsilon_0 \epsilon_n \epsilon_p V_{bi}}{eN_A(\epsilon_n N_A + \epsilon_p N_D)}} \quad (6)$$

$$W_n = \frac{W_p N_A}{N_D}. \quad (7)$$

According to the relations $N_{D[A]} = n_D[n_A]/t_{n[p]}$, t is the thickness of the monolayer in-plane heterojunction and can be read directly from the AFM image ($t_{WSe_2} \approx 0.8$ nm, $t_{WS_2} \approx 0.6$ nm). So $N_D \approx 2.99 \times 10^{14}$ cm⁻³, $N_A \approx 1.73 \times 10^{14}$ cm⁻³. In addition, the modeling predicts the depletion width W_n and W_p to be approximately 1.43 and 2.48 μ m respectively, compared with the estimated value ($W \sim 11.67$ μ m). This implies that the theoretical p - n heterojunction modeling, which is based on the assumption of no free carriers and constant dopant concentration for the intentionally doped inorganic semiconductors with high-carrier mobility [32], is not completely suitable for describing electronic transport in the 2D covalently bonded heterojunction, and remains to be explored.

Considering the heating phenomenon in the practical integrated circuit of the photoelectric devices, we performed temperature-dependent (305 K–405 K) characterization utilizing the KPFM technique, which was conducted in a N₂ atmosphere. Figure 4(a) displays the surface potential mappings of the WSe₂–WS₂–WSe₂ interface at different temperatures. It distinctly shows that the surface potential of WSe₂ declines with temperature, and the WS₂ manifests an opposing tendency. The variation of the surface potential reflects the thermodynamic charges transferring across the WSe₂–WS₂–WSe₂ interface. An n - p to p - n junction transition emerges at the critical point of temperature (T_c , 365 \sim $T_c \sim$ 375 K) [33]. For clarity, we plotted the horizontal profiles of the surface potential distribution at the WSe₂–WS₂–WSe₂ interface, as shown in figure 4(b). It is noteworthy that each of the curves is averaged along the y -axis direction in figure 4(a) at the corresponding temperature. A flat band condition is reached at T_c , where the value of the workfunctions from the WSe₂ and WS₂ sides stay very close, implying that a zero-barrier ohmic contact between WSe₂ and the WS₂ side is formed.

To understand the intrinsic mechanism of the electronic states during the period of the temperature increase, the surface potential profiles of the WSe₂–WS₂ interface in the whole temperature range are plotted in figure 5(a). Each curve is fitted by the sigmoid function as discussed above. The closed Fermi levels of WSe₂ and WS₂ at T_c benefit the thermodynamic behaviors of the carriers traveling through the WSe₂–WS₂ interface. For a detailed view of the dynamic variation of the electric contact between WSe₂ and WS₂, the built-in potential barrier with temperature is derived in figure 5(b). Obviously, the positive value of the contact barrier tends to decline with an increase in temperature, indicating a negative temperature correlation of the built-in

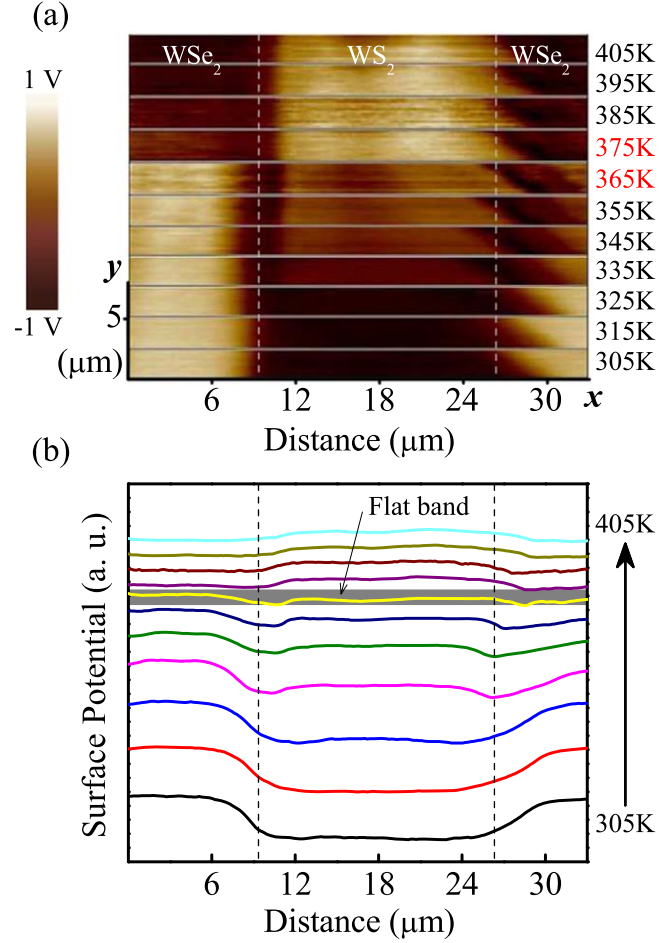


Figure 4. (a) Surface potential images at the WSe₂–WS₂–WSe₂ interface for variable temperature ranging from 305 K–415 K with a step of 10 K. Note that the mapping region is located in the white dashed rectangle marked in figure 2(b). (b) Surface potential distribution at the WSe₂–WS₂–WSe₂ interface within variable temperature.

contact barrier. This shows a decrease in the contact resistance with an increase in the temperature of semiconductor devices, unlike the resistance in the semimetal devices of the 1T' phase [34]. The mostly weakened barrier (~ 0 V) emerges, implying that the electric contact is effectively tailored at T_c . When the temperature is beyond T_c , the contact barrier between the WSe₂ and WS₂ side increases with a negative value. Consequently, the charge injection from WSe₂ to WS₂ is hindered, rendering a relatively opposing diffusion from WS₂ to WSe₂.

Since the specific resistivity inside the semiconductors can be strongly affected by the doping level, we have explored the variation of the intrinsic carrier concentration, which is indirectly displayed by the workfunction profile. As shown in figure 5(c), the workfunction variation of WSe₂ and WS₂ with temperature is deduced. Note that the Fermi levels shift in the opposite direction with the workfunction; the profile shows that both the amount of carriers in the n -type WSe₂ and p -type WS₂ sides decrease with temperature. This phenomenon is inconsistent with the view that the higher the temperature, the greater the chance of the carriers being

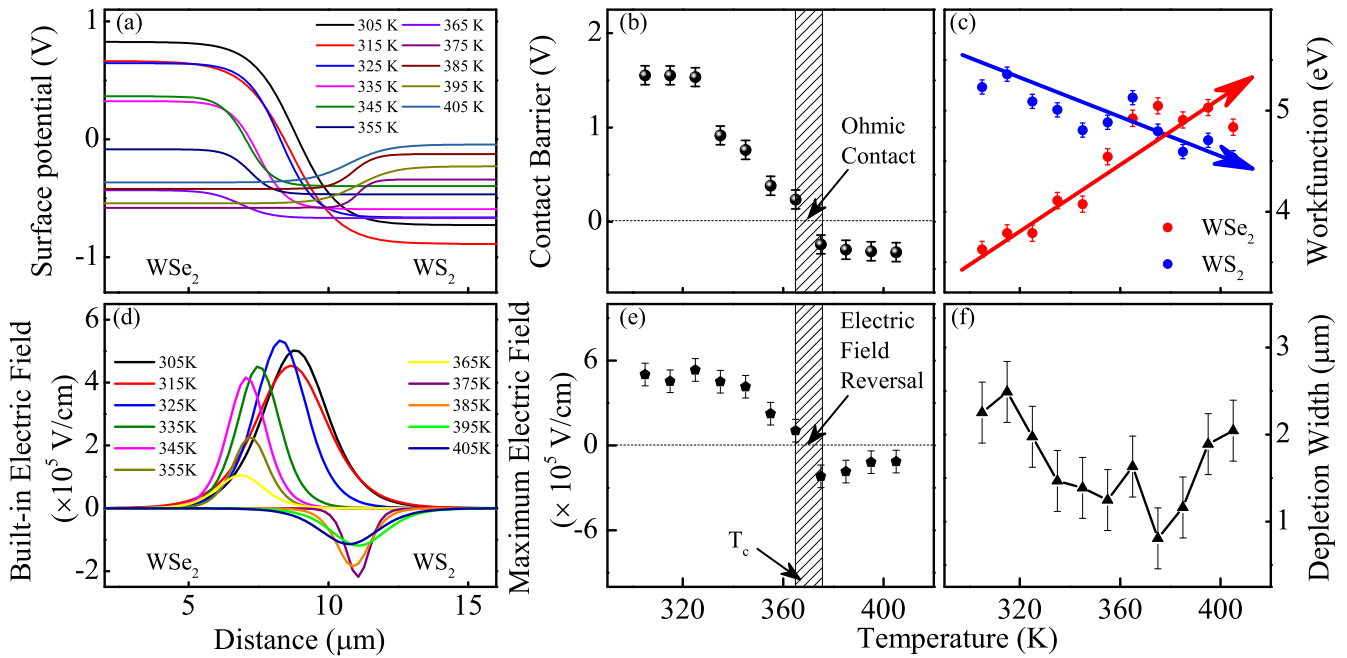


Figure 5. (a) S-fitting curves of the surface potential at the WSe_2 - WS_2 interface at different temperatures. (b) Built-in contact barrier variation and (c) workfunction variations of WSe_2 and WS_2 at different temperatures, respectively. (d) Built-in electric field distribution at different temperatures. (e) Maximum electric field and (f) depletion width plots at different temperatures, respectively. Note that the width of the shadow rectangles in panels (b) and (e) represent the critical temperature.

thermally excited. Bearing in mind that the environment, such as substrate and ambient, has a strong impact on the doping concentration of carriers [35], it can be concluded that the drop in the amount of carriers can thus be attributed to the electron-withdrawing effect induced by the Si/SiO₂ substrate of the WSe_2 - WS_2 heterojunction. [9, 36].

Considering that the electric field poling is sensitive to temperature [37], the spatial distribution of the built-in electric field at different temperatures is obtained by differentiating the work function, as shown in figure 5(d). The pronounced transformation of the built-in electric field can be due to the thermal transferring behaviors that result in the change of electron location at the lattice, which is very susceptible to structural strain along the lattice distribution at the interface. The direction of the built-in electric field gradually reverses at T_c . This evolution of the built-in electric field with the increasing temperature process is assumed to be the difference in the thermal expansion coefficient (TEC) between the WSe_2 and WS_2 materials, which can induce a structural mismatch of the lattice [33]. Previous work has reported that the TEC mismatch would induce a strain effect in the 2D materials [38]. To verify the strain effect during the temperature varying process, the temperature-dependent Raman spectroscopy at the interface of the WSe_2 - WS_2 lateral heterojunction is utilized, as shown in figure S2(a). The peak position behaves as a function of temperature for the frequency modes of WS_2 and WSe_2 , as shown in figure S2(b)-(d), which we conclude to be the contribution from the thermal anharmonic effect and the thermal expansion [38-41]. In addition, there is a discrepancy in the extracted slope of the linear fitting from the Raman modes *versus* temperature, which is consistent with previous

work [42]. These results accordingly confirm that the strain effect is a consequence of the difference between the thermal coefficient of these materials.

Based on equations (5) and (6), the depletion width at variable temperature is deduced in figure 5(f). The width shrinks till it reaches the minimum value at T_c . When the temperature is beyond the T_c , the width of the depletion region gradually increases, which indicates that the unit cells recover their cubic shape. We concluded that this is due to the thermal diffusion of the intrinsically excited carriers. Due to the fact that the generated holes and electrons move towards the opposite direction and approach the border of the depletion region, the depletion width declines.

4. Conclusion

In summary, the *in situ* thermal exploration of the photon-electron and electronic evolution of the type II interface in a monolayer WSe_2 - WS_2 lateral heterojunction was performed. The exciton transition energy relating to the photon-electron interaction experienced a blueshift from pristine materials to the interface, which was attributed to the direct-to-indirect exciton transition of the interband. The coupling strength for the covalently bonded interface was strong which was revealed by the weak shift of the photon energy with temperature. Nevertheless, the evolution of the lattice strain effect was magnified by the obvious variation of the built-in electric field with temperature through the computational methods for extracting the electron distribution. In addition, the electric contact at the interface has shown a negative correlation with temperature that facilitated more carrier spanning behaviors. Our results emphasize the

evolution relation between the light emission and electronic states of the type II interface in lateral heterojunctions, and they contribute to providing universal paths to the evaluation of the electrical contact for fundamental investigation as well as TMDC-based photodioxide devices.

Acknowledgments

This work was financially supported by the National Key R&D Program of China (Grant Nos. 2018YFB0406500 and 2017YFA0303403), the National Natural Science Foundation of China (Grant Nos. 61674057 and 61227902), the Projects of Science and Technology Commission of Shanghai Municipality (Grant Nos. 18JC1412400, 18YF1407200, 18YF1407000, and 15JC1401600), and the Program for Professor of Special Appointment (Eastern Scholar) at Shanghai Institutions of Higher Learning and the Fundamental Research Funds for the Central Universities.

ORCID iDs

Zhigao Hu  <https://orcid.org/0000-0003-0575-2191>

References

- [1] Li M Y *et al* 2015 Epitaxial growth of a monolayer WSe₂-MoS₂ lateral p-n junction with an atomically sharp interface *Science* **349** 524–8
- [2] Zhang X Q, Lin C H, Tseng Y W, Huang K H and Lee Y H 2015 Synthesis of lateral heterostructures of semiconducting atomic layers *Nano Lett.* **15** 410–5
- [3] Ross J S *et al* 2014 Electrically tunable excitonic light-emitting diodes based on monolayer WSe₂ p-n junctions *Nat. Nanotechnology* **9** 268–72
- [4] Zhang K *et al* 2017 Defect-induced epitaxial growth for efficient solar hydrogen production *Nano Lett.* **17** 6676–83
- [5] Zhang K, Kim J K, Ma M, Yim S Y, Lee C-L, Shin H and Park J H 2016 Delocalized electron accumulation at nanorod tips: origin of efficient H₂ generation *Adv. Funct. Mater.* **26** 4527–34
- [6] Song S, Keum D H, Cho S, Perello D, Kim Y and Lee Y H 2016 Room temperature semiconductor-metal transition of MoTe₂ thin films engineered by strain *Nano Lett.* **16** 188–93
- [7] Cho S *et al* 2015 Phase patterning for ohmic homojunction contact in MoTe₂ *Science* **349** 625–8
- [8] Qi D, Wang Q, Han C, Jiang J, Zheng Y, Chen W, Zhang W and Wee A T S 2017 Reducing the schottky barrier between few-layer MoTe₂ and gold *2D Mater.* **4** 045016
- [9] Zheng C *et al* 2017 Direct observation of 2D electrostatics and ohmic contacts in template-grown graphene/WS₂ heterostructures *ACS Nano* **11** 2785–93
- [10] Kong Q, Wang X, Xia L, Wu C, Feng Z, Wang M and Zhao J 2017 Achieving low contact resistance by engineering a metal-graphene interface simply with optical lithography *ACS Appl. Mater. Interfaces* **9** 21573–8
- [11] Bogaert K, Liu S, Chesin J, Titow D, Gratecak S and Garaj S 2016 Diffusion-mediated synthesis of MoS₂/WS₂ lateral heterostructures *Nano Lett.* **16** 5129–34
- [12] Gong Y *et al* 2014 Vertical and in-plane heterostructures from WS₂/MoS₂ monolayers *Nat. Mater.* **13** 1135–42
- [13] Duan X *et al* 2014 Lateral epitaxial growth of two-dimensional layered semiconductor heterojunctions *Nat. Nanotechnol.* **9** 1024–30
- [14] Gong Y *et al* 2015 Two-step growth of two-dimensional WSe₂/MoSe₂ heterostructures *Nano Lett.* **15** 6135–41
- [15] Li Z *et al* 2017 Synthesis of ultrathin composition graded doped lateral WSe₂/WS₂ heterostructures *ACS Appl. Mater. Interfaces* **9** 34204–12
- [16] Chen K, Wan X, Wen J, Xie W, Kang Z, Zeng X, Chen H and Xu J 2015 Electronic properties of MoS₂CWS₂ heterostructures synthesized with two-step lateral epitaxial strategy *ACS Nano* **9** 9868–76
- [17] Zhang C, Li M Y, Tersoff J, Han Y, Su Y, Li L J, Muller D A and Shih C K 2018 Strain distributions and their influence on electronic structures of WSe₂-MoS₂ laterally strained heterojunctions *Nat. Nanotechnology* **13** 152–8
- [18] Lee C H *et al* 2014 Atomically thin P-N junctions with Van Der Waals heterointerfaces *Nat. Nanotechnology* **9** 676–81
- [19] Doan M H, Jin Y, Adhikari S, Lee S, Zhao J, Lim S C and Lee Y H 2017 Charge transport in MoS₂/WSe₂ Van Der Waals heterostructure with tunable inversion layer *ACS Nano* **11** 3832–40
- [20] Chen X, Qiu Y, Yang H, Liu G, Zheng W, Feng W, Cao W, Hu W and Hu P 2017 In-plane mosaic potential growth of large-area 2d layered semiconductors MoS₂-MoSe₂ lateral heterostructures and photodetector application *ACS Appl. Mater. Interfaces* **9** 1684–91
- [21] Hansen W N and Hansen G J 2001 Standard reference surfaces for work function measurements in air *Surf. Sci.* **481** 172–84
- [22] Liang Y, Zhai L, Zhao X and Xu D 2005 Band-gap engineering of semiconductor nanowires through composition modulation *J. Phys. Chem. B* **109** 7120–3
- [23] Duan X *et al* 2016 Synthesis of WS₂xSe_{2-2x} alloy nanosheets with composition-tunable electronic properties *Nano Lett.* **16** 264–9
- [24] Mann J *et al* 2014 2-Dimensional transition metal dichalcogenides with tunable direct band gaps: MoS_{2(1-x)}Se_{2x} monolayers *Adv. Mater.* **26** 1399–404
- [25] Almadori Y, Bendiab N and Grevin B 2018 Multimodal kelvin probe force microscopy investigations of a photovoltaic WSe₂/MoS₂ type-II interface *ACS Appl. Mater. Interfaces* **10** 1363–73
- [26] Ren J, McIsaac K A, Patel R V and Peters T M 2007 A potential field model using generalized sigmoid functions *IEEE Trans. Syst. Man Cybern. B* **37** 477–84
- [27] Corovic S, Lackovic I, Sustaric P, Sustar T, Rodic T and Miklavcic D 2013 Modeling of electric field distribution in tissues during electroporation *Biomed. Eng. Online* **12** 1–27
- [28] Chen K, Wan X, Xie W, Wen J, Kang Z, Zeng X, Chen H and Xu J 2015 Lateral built-in potential of monolayer MoS₂-WS₂ in-plane heterostructures by a shortcut growth strategy *Adv. Mater.* **27** 6431–7
- [29] Cudazzo P, Tokatly I V and Rubio A 2011 Dielectric screening in two-dimensional insulators: implications for excitonic and impurity states in graphane *Phys. Rev. B* **84** 085406
- [30] Lin Y, Ling X, Yu L, Huang S, Hsu A L, Lee Y H, Kong J, Dresselhaus M S and Palacios T 2014 Dielectric screening of excitons and trions in single-layer MoS₂ *Nano Lett.* **14** 5569–76
- [31] Berkelbach T C, Hybertsen M S and Reichman D R 2013 Theory of neutral and charged excitons in monolayer transition metal dichalcogenides *Phys. Rev. B* **88** 045318
- [32] Anderson R L 1962 Experiments on Ge-GaAs heterojunctions *Solid State Electron.* **5** 341–51
- [33] Wen T D and Anastassakis E 1996 Temperature dependence of strains and stresses in undercritical cubic superlattices and heterojunctions *Phys. Rev. B* **53** 8
- [34] Zhou L *et al* 2016 Synthesis of high-quality large-area homogenous 1T' MoTe₂ from chemical vapor deposition *Adv. Mater.* **28** 9526–31

- [35] Bao W, Cai X, Kim D, Sridhara K and Fuhrer M S 2013 High mobility ambipolar Mos₂ field-effect transistors: substrate and dielectric effects *Appl. Phys. Lett.* **102** 042104
- [36] Larentis S, Tolsma J R, Fallahazad B, Dillen D C, Kim K, MacDonald A H and Tutuc E 2014 Band offset and negative compressibility in graphene-MoS₂ heterostructures *Nano Lett.* **14** 2039–45
- [37] Zhang C, Sun D, Liu X, Sheng C X and Vardeny Z V 2017 Temperature-dependent electric field poling effects in CH₃NH₃PbI₃ optoelectronic devices *J. Phys. Chem. Lett.* **8** 1429–35
- [38] Yoon D, Son Y W and Cheong H 2011 Negative thermal expansion coefficient of graphene measured by Raman spectroscopy *Nano Lett.* **11** 3227–31
- [39] Huang X, Gao Y, Yang T, Ren W, Cheng H M and Lai T 2016 Quantitative analysis of temperature dependence of Raman shift of monolayer WS₂ *Sci. Rep.* **6** 32236
- [40] Late D J, Maitra U, Panchakarla L S, Waghmare U V and Rao C N 2011 Temperature effects on the raman spectra of graphenes: dependence on the number of layers and doping *J. Phys.: Condens. Matter* **23** 055303
- [41] Najmaei S, Ajayan P M and Lou J 2013 Quantitative analysis of the temperature dependency in Raman active vibrational modes of molybdenum disulfide atomic layers *Nanoscale* **5** 9758–63
- [42] Pawbake A S, Pawar M S, Jadkar S R and Late D J 2016 Large area chemical vapor deposition of monolayer transition metal dichalcogenides and their temperature dependent raman spectroscopy studies *Nanoscale* **8** 3008–18